

SplatVoxel: History-Aware Novel View Streaming without Temporal Training

Yiming Wang^{1,2*} Lucy Chai² Xuan Luo² Michael Niemeyer² Manuel Lagunas²
 Stephen Lombardi² Siyu Tang¹ Tiancheng Sun²
¹ETH Zurich ²Google

Abstract

We study the problem of novel view streaming from sparse-view videos, which aims to generate a continuous sequence of high-quality, temporally consistent novel views as new input frames arrive. However, existing novel view synthesis methods struggle with temporal coherence and visual fidelity, leading to flickering and inconsistency. To address these challenges, we introduce history-awareness, leveraging previous frames to reconstruct the scene and improve quality and stability. We propose a hybrid splat-voxel feed-forward scene reconstruction approach that combines Gaussian Splatting [22] to propagate information over time, with a hierarchical voxel grid for temporal fusion. Gaussian primitives are efficiently warped over time using a motion graph that extends 2D tracking models to 3D motion, while a sparse voxel transformer integrates new temporal observations in an error-aware manner. Crucially, our method does not require training on multi-view video datasets, which are currently limited in size and diversity, and can be directly applied to sparse-view video streams in a history-aware manner at inference time. Our approach achieves state-of-the-art performance in both static and streaming scene reconstruction, effectively reducing temporal artifacts and visual artifacts while running at interactive rates (15 fps with 350ms delay) on a single H100 GPU.

1. Introduction

Novel view streaming with sparse views is a challenging yet essential problem with applications in augmented and virtual reality (AR/VR). The goal is to reconstruct and render temporally consistent novel views when new frames continuously come in. While recent advances in novel view synthesis, such as 3D Gaussian Splatting (3DGS) [22], enable real-time rendering, they typically require minutes of per-scene optimization using densely sampled views to construct a scene representation. This computational overhead, combined with the need for dense camera coverage, makes

* Work done during an internship at Google.

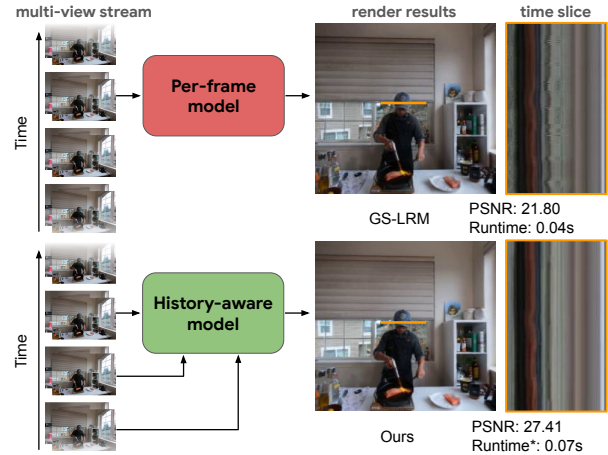


Figure 1. (Top) Per-frame reconstruction methods, which produce an independent scene reconstruction at each time step, are prone to flickering artifacts. (Bottom) In contrast, our **history-aware** novel view streaming model merges previous and current frame information, allowing us to better model occluded regions and improve temporal stability. Our method achieves state-of-the-art visual quality and temporal consistency, and runs in interactive rate (15 fps with a 350ms delay*) on two view inputs of resolution 320×240 .

them impractical for online streaming reconstruction with sparse camera setups, where each frame must be processed within a reasonable time budget for video output. Feed-forward reconstruction methods [5, 14, 79] trained with large-scale scene datasets offer a more efficient alternative by enabling sparse view reconstruction and rendering without per-scene optimization. However, these methods operate on each frame independently at inference time, omitting temporal information. As a result, they usually struggle with flickering artifacts and occlusion handling.

In this paper, we tackle the problem of novel view streaming with *history-awareness*, leveraging information from previous frames. This is particularly crucial in sparse-view settings, where per-frame data is often insufficient and occlusions are common. By incorporating history, we can enhance reconstruction quality and mitigate temporal flickering artifacts, significantly improving the user experience. However, working on multi-view dynamic scene recon-

struction presents its own challenges. Large-scale, multi-view video datasets suitable for training are very limited, and efficiently modeling temporal correspondences is non-trivial. To this end, we present a novel feed-forward scene reconstruction method that effectively leverages historical information for streaming reconstruction without requiring training on the currently limited multi-view video datasets. Our approach introduces a hybrid Splat-Voxel representation that combines the advances of Gaussian Splatting [22] and an efficient sparse voxel transformer. Specifically, we adopt Gaussian Splatting as a moveable point-based representation, enabling real-time splatting-based rendering and facilitating deformation across frames. We warp the historical feed-forward reconstruction of Gaussian Splatting using an efficient motion uplifting algorithm, which leverages existing 2D motion priors from pretrained models [10, 64]. To integrate historical information carried from warped Gaussian primitives with new observations from the current frame, we introduce a sparse voxel transformer with a coarse-to-fine voxel representation, enabling effective information fusion within a temporally shared Euclidean space. Our method achieves state-of-the-art performance in terms of rendering quality and temporal consistency on several multi-view video datasets under the sparse camera setup, and can reach interactive rate (15fps with 350ms delay) under a single H100 GPU. In summary, the main contributions of our paper are as follows:

- We propose a hybrid Splat-Voxel feed-forward reconstruction framework that leverages historical information to enable novel view streaming, without relying on multi-view video datasets for training.
- We develop an efficient sparse voxel transformer with a coarse-to-fine voxel representation, outperforming existing feed-forward Gaussian splatting methods.
- Experiment results demonstrate that our proposed framework enhances novel view synthesis for streaming scene reconstruction with better visual quality and reduced temporal artifacts through history-aware modeling.

2. Related Work

Novel View Synthesis Image-based rendering approaches for novel view synthesis (NVS) predict the appearance of a scene from novel viewpoints given a set of input images. A key design decision is the choice of 3D scene representation to establish correspondences and capture structure. Popular representations include multi-plane images [4, 13, 27, 65, 71, 72, 82], neural fields [40, 56], voxel grids [41, 50, 61], and Gaussian splatting [22]. NVS methods can be broadly divided into those that optimize scene representation at test time and those that directly predict it through a feed-forward network [5, 12, 52, 59, 67, 78]. Recently, transformers have been used to reason about scenes without explicit

3D bias [20, 53, 54] or in combination with differentiable renderers in a hybrid approach [17, 79]. Our method follows the latter paradigm, leveraging a transformer backbone that integrates voxel grids and 3D Gaussians for scene representation while operating in a data-driven feed-forward manner to achieve streaming applications.

Reconstructing Dynamic Scenes Handling dynamic motions in novel view synthesis (NVS) is challenging due to occlusions and the need for temporal consistency. Dynamic scene reconstruction is typically addressed in multi-view setups with fixed cameras [8, 38, 57, 73, 75] or monocular settings where both the camera and scene move [28, 29, 43, 68, 74]. Most methods optimize on the entire video sequences, relying on learned or hand-crafted priors such as optical flow [36, 64], tracking [10], and depth estimation [44, 48, 49, 76] for supervision [28, 74]. To regularize motion, these methods often incorporate basis functions [29, 30, 68] or motion priors [47], while others explicitly model static and dynamic components separately [21, 32, 35]. These techniques support applications such as animation [18, 47, 63], tracking [39, 68], and semantic understanding [33]. Some methods accelerate reconstruction by preserving past reconstructions for faster optimization [25, 62, 69], but they remain computationally expensive and impractical for real-world, sparse-view streaming scenarios. Our method uses pretrained models (specifically, point tracking) for motion priors. However, unlike typical methods that optimize on the entire video sequence, our model operates causally and online, using only previously received frames.

Online 3D Reconstruction Feed-forward approaches achieve online 3D reconstruction by predicting novel views in a single pass without per-scene optimization. However, many rely solely on the current frame [14, 31, 34, 51], neglecting temporal information, which leads to flickering and occlusion artifacts. Some methods [31, 51] train on large-scale dynamic video datasets, often incorporating synthetic data due to the scarcity of real-world multi-view videos. However, they assume access to full sequences at inference, limiting their applicability in real-time settings. Our approach bridges these gaps by combining the efficiency of feed-forward inference with history-awareness. Unlike optimization-based methods, we do not require future frames, and unlike standard feed-forward models, we leverage past frames to improve temporal consistency. By generalizing from static scene training to dynamic video inference without additional temporal supervision, our method enables efficient, real-time novel view streaming from sparse multi-view inputs.

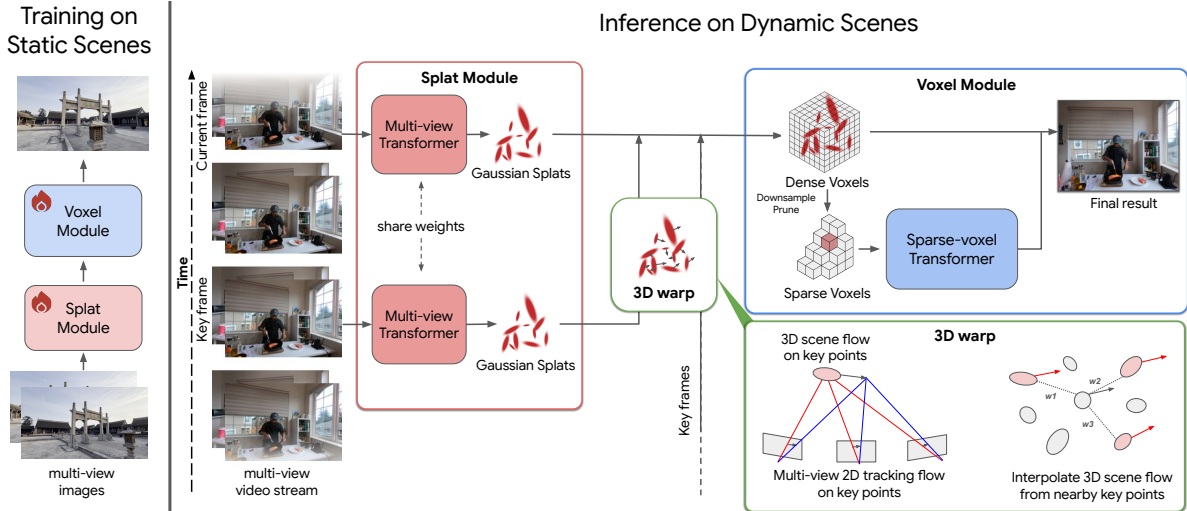


Figure 2. **Method Overview.** Our hybrid SplatVoxel model first extracts input image features using a multi-view transformer, which outputs pixel-aligned Gaussian splats for each input image with associated features. The splat features are then deposited onto a coarse-to-fine voxel grid using the decoded position, and a secondary sparse voxel transformer processes the grid features to output final Gaussian parameters. To merge history, we compute the triangulated scene flow from the input views and perform keypoint guided deformations. These deformed splats can be treated identically to the input-aligned splats, and be similarly deposited into voxel grid to merge the previous state with the current state. Our system is trained only on static scenes, and can generalize to dynamic scenes during inference.

Table 1. **Method Comparison.** Unlike existing baselines, our framework uniquely supports the three key requirements of the novel view streaming task targeted in this paper: fast reconstruction with interactive rate, sparse view inputs, and history awareness. In particular, our streaming approach only uses *past* frames, in contrast to DeformableGS [77] and DeformableNerf [43] that optimize over *all** frames. The history-awareness in our model mitigates temporal flickering and occlusion artifacts, and is also able to support unlimited sequence lengths.

| Method | Interactive Speed | Sparse-view Input | History Awareness |
|---------------------|-------------------|-------------------|-------------------|
| NeRF [40] | × | × | × |
| InstantNGP [41] | × | × | × |
| 3DGS [22] | × | × | × |
| DeformableGS [77] | × | ✓ | ✓* |
| DeformableNerf [43] | × | ✓ | ✓* |
| PixelSplat [5] | × | ✓ | × |
| GS-LRM [79] | ✓ | ✓ | × |
| Quark [14] | ✓ | ✓ | × |
| Ours | ✓ | ✓ | ✓ |

3. Online Novel View Streaming

Given **sparse** (e.g., 2–4 views) RGB video streams from fixed and calibrated cameras, we aim to achieve **online** novel view synthesis, using only temporal information from past frames. The key objectives for our approach include efficient reconstruction (i.e. > 10 fps interactive rate) and effective reuse of past information. History awareness is essential for our task given the sparse coverage of the input cameras, which can lead to artifacts such as temporal flickering and degraded reconstruction in occluded regions. Rather than processing each frame independently, using information from prior frames improves the per-frame reconstruction quality and ensures temporal consistency.

Challenges Optimization-based methods [2, 22, 40, 41, 73] are not well-suited for this task, as they require extensive optimization over entire video sequences. Additionally, they perform poorly with sparse views and face challenges in representing long video sequences due to memory and capacity constraints. Recent feed-forward reconstruction methods [5, 6, 14, 79] have shown promise in efficient sparse-view reconstruction of static scene by utilizing large networks trained on large-scale multi-view datasets. However, their lack of explicit temporal modeling makes them prone to temporal flickering and occlusions in video inputs, resulting in suboptimal performance for our novel view streaming task.

Table 1 highlights the differences among these prior methods, none of which address novel view streaming or incorporate historical information. Integrating history-awareness into existing frameworks is particularly challenging. A major obstacle in training history-aware feed-forward networks is the limited availability of high-quality multi-view video datasets. Moreover, naive approaches, such as continuously warping historical scene reconstructions to later frames, fail to capture newly appearing objects and changes in appearance—not to mention that accurate 3D scene motion estimation from sparse multi-view RGB inputs remains challenging and prone to accumulated errors, ultimately degrading reconstruction fidelity.

Our Solution To address these challenges, we propose a novel feed-forward reconstruction framework that generalizes to temporal video streams at inference time, despite being trained solely on multi-view static scenes. Our approach

leverages a hybrid point-voxel representation, combining the flexibility of point-based methods with the structured spatial organization of voxels, drawing inspiration from hybrid Lagrangian-Eulerian methods [19] commonly used in physics simulation.

Our two-stage pipeline first constructs a movable point-based (Lagrangian) representation, which is then transferred into a voxel-based (Eulerian) representation. This design naturally extends static scene reconstruction to history-aware dynamic scene reconstruction, where historical information is retained within the Lagrangian component and continuously integrated with new data on the global Eulerian grid, following the principles of hybrid Lagrangian-Eulerian methods.

For our novel view streaming task, we employ Gaussian Splatting [22] as the Lagrangian component and a coarse-to-fine sparse voxel grid as the Eulerian component. A multi-view transformer learns to generate Lagrangian Gaussian primitives from multi-view RGB images, while a voxel transformer fuses information within the Eulerian grid in latent space. After training on a large-scale static scene dataset, our method enables online novel view streaming without additional temporal training. This is achieved by warping Gaussian primitives using an embedded deformation graph [60] derived from uplifted 2D tracks [10] and integrating the warped primitives with the current frame using the voxel transformer.

4. Method

In this section, we describe our SplatVoxel feed-forward scene reconstruction framework (Sec 4.1), and how it can generalize at inference time for zero-shot history-aware 4D novel view streaming (Sec 4.2).

4.1. Efficient SplatVoxel Transformer

Our two-stage feed-forward reconstruction model fuses information across 2D and 3D domains by first using a multi-view transformer to process 2D images into Gaussian splat primitives (we refer to a 3D Gaussian primitive as a ‘‘splat’’ for brevity here and in the following sections). We then deposit the splats on a voxel grid and train a sparse coarse-to-fine voxel transformer to refine the Gaussian primitives.

4.1.1. Multi-view Transformer

Given N RGB images of resolution $H \times W$ with known camera parameters, we extract multi-view latent features and train a transformer following GS-LRM [79]. We concatenate the RGB value with per-pixel Plücker ray embeddings [45]. Next, we extract features from non-overlapping $p \times p$ image patches [11] using a single-layer CNN, resulting in patch features with channel dimension of C . The resulting multi-view image patch features are concatenated into a set of $N \times HW/p^2$ tokens, which we denote as $\{\mathbf{X}\}$.

The multi-view (MV) transformer [66] then processes image tokens $\{\mathbf{X}\}$ to capture the underlying geometric and appearance, producing a set of latent features $\{\mathbf{Z}\}$:

$$\{\mathbf{Z}\} = \text{Transformer}_{MV}(\{\mathbf{X}\}) \quad (1)$$

We unpatchify the processed latent features to Gaussian primitives with a linear layer applied to each latent:

$$\{\mathbf{G}_k, \mathbf{F}_k\} = \text{Linear}(\{\mathbf{Z}\}) \quad (2)$$

where \mathbf{G}_k is a Gaussian primitive aligned with each input pixel ($k = 1, \dots, NHW$) which can be rendered using Gaussian splatting [22], and \mathbf{F}_k is an associated feature vector for each Gaussian primitive.

4.1.2. Splat-to-Voxel Transfer

While previous feed-forward Gaussian Splatting methods [5, 6, 79] typically represent the scene by simply concatenating per-pixel splats predicted from different views, we propose a 3D-aware refinement step on splats \mathbf{G}_k and associated features \mathbf{F}_k by leveraging an intermediate voxel-based representation. This Splat-to-Voxel Transfer is achieved by first performing *Splat Depositing* onto a voxel grid, followed by *Splat Fusion* in Euclidean space to produce the input for our sparse voxel transformer.

Splat Depositing Given voxel grid V , we deposit each Gaussian primitive \mathbf{G}_k to the set of $\{\mathbf{M}_k\}$ of nearest voxels based on the position μ_k using a distance kernel \mathcal{K} . That is, for voxel V_j , its weight associated with \mathbf{G}_k is:

$$w_{jk} = \begin{cases} \frac{\mathcal{K}(\mu_k - \mathbf{x}_j)}{\sum_{j' \in \{\mathbf{M}_k\}} \mathcal{K}(\mu_k - \mathbf{x}_{j'})}, & \text{if } j \in \{\mathbf{M}_k\}, \\ 0 & \text{otherwise.} \end{cases} \quad (3)$$

where \mathbf{x}_j represents the center of the j -th voxel (details in supplementary). We choose the adjacent 8 voxels for each splat in our implementation. We note that the same splat depositing procedure can be used for Gaussian primitives originating from multi-view images, or warped from previous frames as will be detailed in Sec. 4.2. This seamlessly integrates all incoming splats which will be used to generate refined primitives with the downstream voxel transformer.

Splat Fusion Each voxel V_j then accumulates the deposited splat attributes using opacity α as weighting. The corresponding voxel attribute \mathbf{E}_j at voxel V_j is then the normalized weighted sum of the splat features \mathbf{F}_k in the voxel:

$$\mathbf{E}_j = \frac{1}{\mathbf{W}_j} \sum_{k \in \{\mathbf{G}_k\}} w_{jk} \alpha_k \mathbf{F}_k, \quad \mathbf{W}_j = \sum_{k \in \{\mathbf{G}_k\}} w_{jk} \alpha_k \quad (4)$$

where w_{jk} is interpolation weight computed in Eqn. 3. We use the notation $k \in \{\mathbf{G}_k\}$ to denote an index into the set of all primitives, with associated weight, opacity, and feature.

Coarse-to-fine voxel hierarchy Once the splat features are deposited onto the voxels, we form the coarse-to-fine voxel hierarchy. Using the previously computed voxel features \mathbf{E}_j as the fine voxel features, we now compute coarse voxel features \mathbf{E}_i^c . Let \mathbf{N}_i be the set of fine voxels associated i -th coarse voxel. We derive coarse voxel features using a shallow multi-layer perceptron (MLP) and set coarse voxel weights as the sum of the associated fine voxel weights:

$$\mathbf{E}_i^c = \text{MLP}_{coarse}([\mathbf{E}_j \mid j \in \mathbf{N}_i]), \quad \mathbf{W}_i = \sum_{j \in \mathbf{N}_i} \mathbf{W}_j \quad (5)$$

We leverage geometric cues from coarse voxel weights \mathbf{W}_i , which encapsulate the spatial distribution and opacity of Gaussian primitives within each voxel, to efficiently cull empty and insignificant regions of the scene. We sort the coarse-level voxels by their voxel weights and retain only the top 20% with the largest weights as a sparse voxel representation of the scene. This sparsification is crucial for the downstream voxel transformer, and reduces the input token count to fewer than $10K$, which allows the voxel transformer to run in 15 ms.

4.1.3. Sparse Voxel Transformer

From coarse voxel features, we treat each voxel feature as a token and reshape to 1D vectors. We train a transformer to process the set of coarse voxel features \mathbf{E}^c :

$$\{\mathbf{O}^c\} = \text{Transformer}_{voxel}(\{\mathbf{E}^c\}) \quad (6)$$

The processed latent features $\{\mathbf{O}^c\}$ are then replicated from the coarse voxel grids within their corresponding fine voxel grids, producing latent features $\{\mathbf{O}\}$ at the fine voxel resolution. A shallow MLP subsequently generates refined Gaussian primitives by integrating the initial fine-level voxel attributes \mathbf{E}_j with the fine-level transformer latent \mathbf{O}_j .

$$\mathbf{G}'_j = \text{MLP}_{fine}([\mathbf{O}_j, \mathbf{E}_j]) \quad (7)$$

where $\mathbf{G}'_j \in \mathbb{R}^l$ represents the predicted Gaussian primitives around the sparsified fine-level voxel grids, with l denoting the number of rendering parameters.

4.1.4. Training

We train the SplatVoxel feed-forward networks on multi-view static scene datasets [37, 82] using a photometric loss combining Mean Squared Error (MSE) and perceptual LPIPS [81]:

$$\mathcal{L} = \mathcal{L}_{\text{MSE}}(\hat{I}, I) + \lambda \mathcal{L}_{\text{LPIPS}}(\hat{I}, I) \quad (8)$$

where \hat{I} denotes ground-truth target image and I the corresponding rendered target image from the predicted Gaussian primitives, which come from either the multi-view

Table 2. **Re10K Reconstruction Metrics.** We train our model on the RealEstate10K dataset and compare it with feed-forward Gaussian Splatting methods. Baseline metrics are obtained from their official papers.

| Method | PSNR \uparrow | SSIM \uparrow | LPIPS \downarrow |
|----------------|-----------------|-----------------|--------------------|
| pixelSplat [5] | 26.09 | 0.863 | 0.136 |
| MVSplat [6] | 26.39 | 0.869 | 0.128 |
| GS-LRM [79] | 28.10 | 0.892 | 0.114 |
| Ours | 28.47 | 0.907 | 0.078 |



Figure 3. **Static scene reconstruction.** Qualitative comparison of our method with recent feed forward GS-LRM [79] on RealEstate10k [82]. Our method preserves high fidelity reconstructions and sharp details.

transformer or voxel transformer. We first train the multi-view transformer, then jointly both multi-view and voxel transformers together. We set λ to 0.5 for the multi-view transformer and 4.0 for the voxel transformer. Training details are provided in the supplementary.

4.2. History-aware Streaming Reconstruction

In this section, we describe how our trained feed-forward SplatVoxel transformer enables zero-shot history-aware novel view streaming, without training on dynamic scenes.

4.2.1. 3D Warping

Due to scene motion, directly using Gaussian primitives from past frames results in lagging artifacts and fails to capture newly appearing objects. Therefore, we use 2D motion cues from pre-trained models to warp 3D Gaussian primitives from past frames to the current frame.

Triangulation Given a Gaussian primitive with an initial position $\mu_{t'}$ at a previous frame t' , we estimate its corresponding 3D position μ_t at the current frame t by performing triangulation on the 2D correspondence obtained by a pretrained 2D point tracking model [10]. In detail, we first compute its 2D projection $\{\mathbf{p}_t^i \mid i = 1 \dots N\}$ across N input views. We then operate 2D point tracking on the projection points to obtain its corresponding 2D pixel position \mathbf{p}_t^i in

Table 3. **Novel View Streaming Metrics.** We compare reconstruction quality of our model to prior methods. Our model differs from these baselines by being history-aware, in contrast to per-frame or temporal methods, and feed-forward rather than optimization-based. Our model outperforms baselines in reconstruction quality and ranks second in temporal smoothness (flicker), whereas the best-ranking baseline in flicker suffers a steep drop in image quality. We report the average running time of processing a single frame on Neural3DVideo at the resolution of 320×240 . GS-LRM and Ours are tested on a single H100 card. 3DGS, 3DGStream, and 4DGS are tested on a single A100* GPU due to limitations with the H100 card. While the efficiency of these optimization-based methods can be enhanced, they still do not achieve a frame rate of 1 FPS. The **best** and **second-best** results are highlighted for clarity.

| Category | Method | Time (s) | 4-view LongVolumetricVideo [75] | | | | 2-view Neural3DVideo [26] | | | |
|----------------------------|----------------|--|---------------------------------|-----------------|--------------------|----------------------|---------------------------|-----------------|--------------------|----------------------|
| | | | PSNR \uparrow | SSIM \uparrow | LPIPS \downarrow | Flicker \downarrow | PSNR \uparrow | SSIM \uparrow | LPIPS \downarrow | Flicker \downarrow |
| Per-frame Optimization | 3DGS [22] | 9.8* | 18.588 | 0.6368 | 0.4334 | 61.686 | 21.02 | 0.6234 | 0.4989 | 43.51 |
| | 3DGStream [62] | 3.8* | 16.970 | 0.4405 | 0.5040 | 12.436 | 14.24 | 0.3542 | 0.6016 | 6.554 |
| Temporal Optimization | 4DGS [73] | 6.0* | 18.754 | 0.6361 | 0.3554 | 6.528 | 23.16 | 0.7812 | 0.2079 | 2.746 |
| Per-frame Feed Forward | GS-LRM [79] | 0.04 | 25.491 | 0.8558 | 0.1377 | 8.463 | 21.80 | 0.8488 | 0.1278 | 5.714 |
| History-aware Feed Forward | Ours | 0.07 (non-keyframe) 0.35 (keyframe) | 25.564 | 0.8645 | 0.1242 | 7.782 | 27.41 | 0.8863 | 0.1040 | 2.916 |

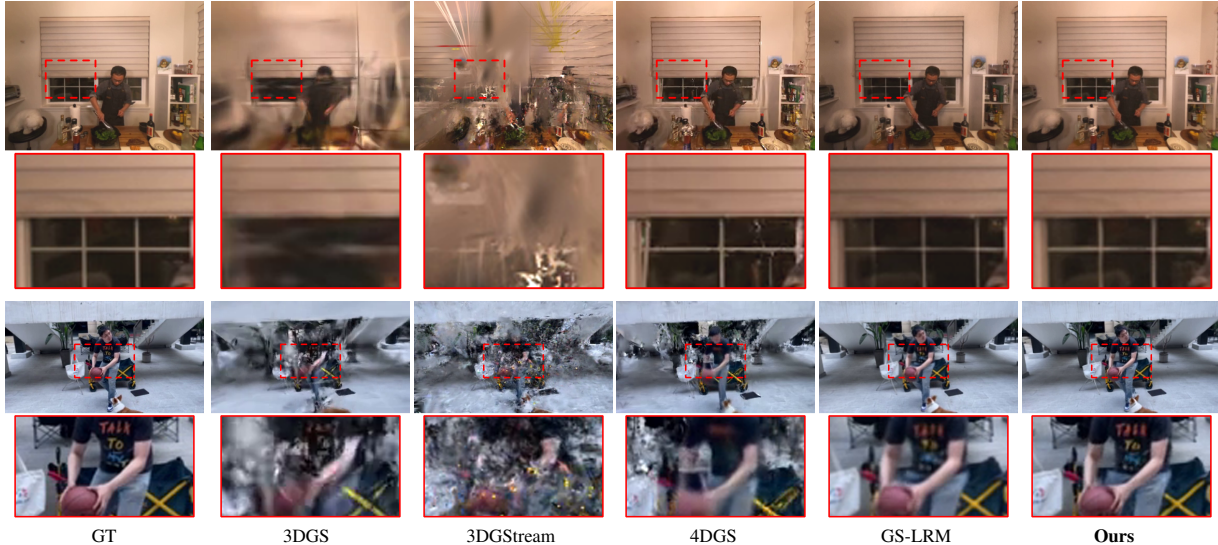


Figure 4. **Streaming Reconstruction.** We compare against per-frame methods (3DGS and GS-LRM) and temporal methods (4DGS and 3DGStream) on LongVolumetricVideo [75] with 4 input views and Neural3DVideo [26] with 2 input views. 3DGS and 3DGStream struggle with sparse input views, while 4DGS is susceptible to occlusion artifacts. GS-LRM is not designed to handle temporal sequences and prone to flicker, while our method mitigates flickering and produces realistic geometry especially in challenging occluded areas.

the current frame. The 3D position is subsequently recovered by finding the closest point to the N camera rays originating from the 2D projections \mathbf{p}_i^j , which can be formulated as the following least-squares optimization problem:

$$\mathbf{x}_c, \lambda_i = \arg \min_{\mathbf{x}, \lambda_i} \sum_i \|(\mathbf{o}_i + \lambda_i \mathbf{d}_i) - \mathbf{x}\|^2 \quad (9)$$

where \mathbf{o}_i and \mathbf{d}_i denote the origin and direction of the i -th camera ray, respectively, and λ_i is a scalar representing the depth along the ray. This least-squares problem can be further converted into solving a linear equation as

$$\left(\sum_i \gamma_i (I_3 - \mathbf{d}_i \mathbf{d}_i^T) \right) \mathbf{x} = \sum_i \gamma_i (I_3 - \mathbf{d}_i \mathbf{d}_i^T) \mathbf{o}_i \quad (10)$$

where I_3 denotes the three-dimensional identity matrix, and γ_i is a visibility mask that indicates whether the projected

2D point is visible throughout the motion occurring in that view. The visibility mask is obtained through a combination of 2D tracking occlusion checks and a depth-based visibility verification, which involves comparing the rendered depth from Gaussian primitives with the projection depth to determine whether the point is visible in front of the surface.

Embedded Deformation Graph While the algorithm above can estimate 3D motion for any splat, doing so for all primitives is computationally expensive due to 2D tracking, and lacks robustness when splats are occluded. Instead, we use an embedded deformation graph [24, 42, 60] to introduce a spatial continuity prior during online motion estimation. We begin by selecting a subset of anchor splats that are consistently visible across multiple views, using farthest sampling [46]. We then construct the embedded deformation graph using a K-nearest neighbors (KNN) approach,

binding each splat to its K -nearest splats and computing blend weights based on distance. To warp splats from the previous frame, we computed embedded deformations on the anchor splats using triangulation, and then propagate motion to all primitives through Linear Blend Skinning. For efficiency, we only maintain primitives from a set of past keyframes, and the contribution of these primitives are smoothly adjusted as older keyframes are replaced by newer ones to ensure seamless temporal transitions. Due to time constraints from querying 2D tracking model, in practice we use two keyframes placed 5 frames apart, each lasting for 10 frames.

4.2.2. Error-aware Temporal Fusion

During online reconstruction, we incorporate both historical Gaussian primitives warped from keyframes and new Gaussian primitives predicted from multi-view observation at the current frame. All of the collected Gaussian primitives are deposited to voxels (Sec. 4.1.2) and then processed by the voxel transformer (Sec. 4.1.3), producing refined, history-aware Gaussian primitives.

To further mitigate artifacts resulting from warping inaccuracies of historical primitives (e.g. warping error, appearance variation, or new objects), we use an adaptive fusion weighting mechanism during splat fusion based on the per-pixel error between the past and current frame splats when rendered to the input views. In more detail, each historical splat is projected onto the input views to assess whether it produces a higher rendering error and appears in front of the rendered depth of the current frame splats. If a historical splat results in increased error in more than half of the input views, we set its fusion weight to zero to suppress unreliable contributions. Concurrently, current frame splats predicted from the multi-view transformer that increase rendering error are assigned zero weight. To enhance temporal continuity, we retain 50% of the voxel attributes from the past keyframe in static areas.

5. Experiments

In this section, we present evaluations of novel view synthesis on both static and dynamic scenes, along with ablation studies on framework design.

5.1. Feed-forward Novel View Synthesis

We first compare our proposed two-stage feed-forward networks with other feed-forward reconstruction methods on the RealEstate10k [82], following the training and testing setup in [5]. Since GS-LRM is not open-source, we re-implement it and report its reproduced performance. Table 2 presents a quantitative comparison based on commonly used novel view synthesis metrics, including Peak Signal-to-Noise Ratio (PSNR), Structural Similarity Index Measure (SSIM) [70], and the perceptual met-

Table 4. **DL3DV Reconstruction Metrics.** We compare our approach with the state-of-the-art feed-forward Gaussian splatting method GS-LRM [37] and present ablation studies on our model designs.

| Method | PSNR \uparrow | SSIM \uparrow | LPIPS \downarrow | Time (ms) |
|---------------------------|-----------------|-----------------|--------------------|-----------|
| GS-LRM | 28.59 | 0.925 | 0.063 | 52.8 |
| Naive Baseline (Mean GS) | 12.57 | 0.357 | 0.741 | 33.8 |
| Ours (w/o Coarse-to-fine) | 20.62 | 0.587 | 0.247 | 48.6 |
| Ours (w/o Sparse Voxel) | 29.69 | 0.926 | 0.060 | 72.0 |
| Ours (3D CNN Downsample) | 29.44 | 0.922 | 0.061 | 82.1 |
| Ours (w/o Splat Feature) | 29.40 | 0.924 | 0.061 | 49.2 |
| Ours (Full) | 30.34 | 0.934 | 0.054 | 52.5 |



Figure 5. **Reconstruction Close-ups.** We show zoomed-in novel view reconstructions of GS-LRM and our model on dynamic scene datasets. Our model better handles occlusion boundaries with sharper detail.

ric LPIPS [80]. As shown in Fig. 3, our method captures finer details, such as thin structures (e.g., chairs) and reflections, outperforming the state-of-the-art feed-forward Gaussian splatting method, GS-LRM [79].

Additionally, we conduct quantitative comparison with GS-LRM on the DL3DV dataset [37] (Table 4). Our method outperforms GS-LRM by approximately 2dB in PSNR while maintaining a comparable transformer capacity with similar inference time, and using the same training setup. Qualitative comparisons and training details are provided in the Supplementary Document.

5.2. Novel View Streaming

We compare our method with baselines on the novel view streaming task on two dynamic scene datasets, Neural3DVideo [26] and LongVolumetricVideo [75]. We use 2 input views and 290 frames for the six sequences in Neural3DVideo, and 4 input views with 1500 frames for the two sequences in LongVolumetricVideo. For quantitative evaluation, we use a temporal metric to measure flicker in the rendered streaming videos in addition to the aforementioned per-frame novel view reconstruction metrics. Temporal flickering is measured using feature-space differences

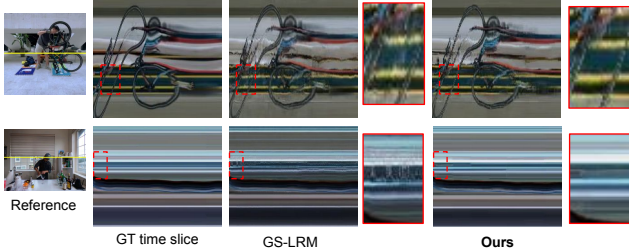


Figure 6. **Temporal Slice Comparison.** We extract a horizontal line in the ground truth and generated videos to visualize temporal stability. Applying GS-LRM independently per frame is more prone to flickering, while our method achieves greater stability and is more robust to occlusion.

over time. Given the predicted frames I_t and ground truth frames I_t^* , we extract deep features using a pretrained VGG network [55] $\phi(\cdot)$:

$$\text{Flicker}_t = |D_t - D_t^*| \quad (11)$$

where $D_t = \|\phi(I_t) - \phi(I_{t-1})\|_2$ and $D_t^* = \|\phi(I_t^*) - \phi(I_{t-1}^*)\|_2$ represent the temporal feature differences for the predicted and ground truth frames at frame t , respectively. The final flicker score is computed by averaging Flicker_t over the entire sequence. Lower values indicate smoother temporal consistency.

Compared to our proposed history-aware feed-forward method, other baseline methods can be classified into three categories: per-frame optimization, temporal optimization, and per-frame feed-forward reconstruction. As presented in Table 3, our method achieves the highest per-frame novel view synthesis performance across all three evaluation metrics on both datasets with the second-best flicker scores. Notably, our approach significantly enhances novel view synthesis results on the Neural3DVideo dataset, where only two input views are available, demonstrating its robustness in handling extremely sparse input settings. In comparison to the state-of-the-art per-frame feed-forward method GS-LRM, our approach qualitatively reconstructs geometry and appearance with greater accuracy and finer details (Fig. 4), and we show close-ups of the reconstruction in Fig. 5. Our method reduces flickering through history-aware modeling, visualized with temporal slices (Fig. 6). Although 4D Gaussian Splatting achieves a better flicker metric, the novel view quality is substantially worse compared to ours. Moreover, its time-consuming temporal optimization is impractical for our target application, which focuses on online processing of arbitrarily long sequences.

5.3. Ablation Studies

We show model ablations on DL3DV in Table 4. Naive mean averaging of Gaussian attributes in each voxel significantly degrades results. The absence of a coarse-to-fine setup limits the capacity of the output Splats, and with-

Table 5. **Ablation Studies on Temporal Components.**

| Method | PSNR \uparrow | SSIM \uparrow | LPIPS \downarrow | Flicker \downarrow |
|------------------------|-----------------|-----------------|--------------------|----------------------|
| w/o History | 27.17 | 0.890 | 0.107 | 5.91 |
| w/o 3D warping | 27.12 | 0.884 | 0.107 | 6.09 |
| w/o Error-aware Fusion | 26.73 | 0.874 | 0.109 | 3.01 |
| Full Model | 27.41 | 0.886 | 0.104 | 2.92 |

out sparsification, we downsampled the grid to 0.75x its original resolution to avoid exceeding memory capacity for the voxel transformer, both leading to poorer reconstruction quality. We also experiment using a 3D CNN to down-sample the voxel grid instead of our proposed coarse-to-fine sparse voxel grid, which is ~ 1 dB worse than our final result and much slower. We also find splat features helpful, operating on splat parameters directly leads to ~ 1 dB drop in PSNR.

We performed ablation studies on the Neural3DVideo dataset to evaluate our streaming reconstruction components, as shown in Table 5. Removing historical Gaussians fails to resolve temporal flicker. Disabling 3D warping led to abrupt keyframe changes and increased reconstruction errors. Eliminating error-aware fusion degraded reconstruction quality due to warping artifacts and other errors.

6. Conclusion

In summary, we introduce a novel approach that leverages information from previous frames to enhance novel view streaming with sparse cameras. Our proposed SplatVoxel framework employs a hybrid representation by modeling scenes with Gaussian primitives and fusing them across frames using sparse voxel grids. This design enables training only on static scenes while supporting zero-shot inference on multi-view video streams via explicit 3D scene flow warping. As a result, our method achieves state-of-the-art performance on multiple multi-view video datasets under sparse camera setups and runs at interactive rates on a single H100 GPU.

While our approach marks an important step toward real-time novel view streaming, it does have limitations. Using pretrained 2D tracking models can be slow and prone to errors in challenging scenarios. Moreover, the current framework still performs a partial 3D reconstruction at each frame rather than incrementally updating previous reconstructions. Future work can explore strategies to leverage historical information without explicit tracking and incrementally refine prior reconstructions, potentially prioritizing regions with higher reconstruction errors. More efficient use of historical reconstructions could also improve the handling of high-resolution novel view streaming. These avenues promise to further enhance the efficiency and quality of history-aware novel view streaming.

Acknowledgement. We would like to express our gratitude to John Flynn, Kathryn Heal, Lynn Tsai, Srinivas Kaza, and Tooba Imtiaz for their helpful discussions, as well as Clément Godard, Jason Lawrence, Michael Broxton, Peter Hedman, Ricardo Martin-Brualla, and Ryan Overbeck for their valuable comments.

References

- [1] Jimmy Lei Ba, Jamie Ryan Kiros, and Geoffrey E Hinton. Layer normalization. *arXiv preprint arXiv:1607.06450*, 2016. 1
- [2] Jonathan T Barron, Ben Mildenhall, Matthew Tancik, Peter Hedman, Ricardo Martin-Brualla, and Pratul P Srinivasan. Mip-nerf: A multiscale representation for anti-aliasing neural radiance fields. In *Proceedings of the IEEE/CVF international conference on computer vision*, pages 5855–5864, 2021. 3
- [3] James Bradbury, Roy Frostig, Peter Hawkins, Matthew James Johnson, Chris Leary, Dougal Maclaurin, George Necula, Adam Paszke, Jake VanderPlas, Skye Wanderman-Milne, and Qiao Zhang. JAX: composable transformations of Python+NumPy programs, 2018. 1
- [4] Michael Broxton, John Flynn, Ryan Overbeck, Daniel Erickson, Peter Hedman, Matthew Duvall, Jason Dourgarian, Jay Busch, Matt Whalen, and Paul Debevec. Immersive light field video with a layered mesh representation. *ACM Transactions on Graphics (TOG)*, 39(4):86–1, 2020. 2
- [5] David Charatan, Sizhe Lester Li, Andrea Tagliasacchi, and Vincent Sitzmann. pixelsplat: 3d gaussian splats from image pairs for scalable generalizable 3d reconstruction. In *Proceedings of the IEEE/CVF Conference on Computer Vision and Pattern Recognition*, pages 19457–19467, 2024. 1, 2, 3, 4, 5, 7
- [6] Yuedong Chen, Haofei Xu, Chuanxia Zheng, Bohan Zhuang, Marc Pollefeys, Andreas Geiger, Tat-Jen Cham, and Jianfei Cai. Mvsplat: Efficient 3d gaussian splatting from sparse multi-view images. In *European Conference on Computer Vision*, pages 370–386. Springer, 2024. 3, 4, 5, 2
- [7] Jaeyoung Chung, Jeongtaek Oh, and Kyoung Mu Lee. Depth-regularized optimization for 3d gaussian splatting in few-shot images. In *Proceedings of the IEEE/CVF Conference on Computer Vision and Pattern Recognition*, pages 811–820, 2024. 2
- [8] Alvaro Collet, Ming Chuang, Pat Sweeney, Don Gillett, Dennis Evseev, David Calabrese, Hugues Hoppe, Adam Kirk, and Steve Sullivan. High-quality streamable free-viewpoint video. 34(4), 2015. 2
- [9] Tri Dao, Dan Fu, Stefano Ermon, Atri Rudra, and Christopher Ré. Flashattention: Fast and memory-efficient exact attention with io-awareness. *Advances in neural information processing systems*, 35:16344–16359, 2022. 1
- [10] Carl Doersch, Yi Yang, Mel Vecerik, Dilara Gokay, Ankush Gupta, Yusuf Aytar, Joao Carreira, and Andrew Zisserman. TAPIR: Tracking any point with per-frame initialization and temporal refinement. In *Proceedings of the IEEE/CVF International Conference on Computer Vision*, pages 10061–10072, 2023. 2, 4, 5, 1
- [11] Alexey Dosovitskiy, Lucas Beyer, Alexander Kolesnikov, Dirk Weissenborn, Xiaohua Zhai, Thomas Unterthiner, Mostafa Dehghani, Matthias Minderer, Georg Heigold, Sylvain Gelly, et al. An image is worth 16x16 words: Transformers for image recognition at scale. *arXiv preprint arXiv:2010.11929*, 2020. 4
- [12] Yilun Du, Cameron Smith, Ayush Tewari, and Vincent Sitzmann. Learning to render novel views from wide-baseline stereo pairs, 2023. 2
- [13] John Flynn, Ivan Neulander, James Philbin, and Noah Snavely. Deepstereo: Learning to predict new views from the world’s imagery. In *Proceedings of the IEEE conference on computer vision and pattern recognition*, pages 5515–5524, 2016. 2
- [14] John Flynn, Michael Broxton, Lukas Murmann, Lucy Chai, Matthew DuVall, Clément Godard, Kathryn Heal, Srinivas Kaza, Stephen Lombardi, Xuan Luo, et al. Quark: Real-time, high-resolution, and general neural view synthesis. *ACM Transactions on Graphics (TOG)*, 43(6):1–20, 2024. 1, 2, 3
- [15] Dan Hendrycks and Kevin Gimpel. Gaussian error linear units (gelus). *arXiv preprint arXiv:1606.08415*, 2016. 1
- [16] Alex Henry, Prudhvi Raj Dachapally, Shubham Pawar, and Yuxuan Chen. Query-key normalization for transformers. *arXiv preprint arXiv:2010.04245*, 2020. 1
- [17] Yicong Hong, Kai Zhang, Jiuxiang Gu, Sai Bi, Yang Zhou, Difan Liu, Feng Liu, Kalyan Sunkavalli, Trung Bui, and Hao Tan. Lrm: Large reconstruction model for single image to 3d. *arXiv preprint arXiv:2311.04400*, 2023. 2
- [18] Yi-Hua Huang, Yang-Tian Sun, Ziyi Yang, Xiaoyang Lyu, Yan-Pei Cao, and Xiaojuan Qi. Sc-gs: Sparse-controlled gaussian splatting for editable dynamic scenes. In *Proceedings of the IEEE/CVF conference on computer vision and pattern recognition*, pages 4220–4230, 2024. 2
- [19] Chenfanfu Jiang, Craig Schroeder, Joseph Teran, Alexey Stomakhin, and Andrew Selle. The material point method for simulating continuum materials. In *Acm siggraph 2016 courses*, pages 1–52. 2016. 4
- [20] Haiyan Jin, Hanwen Jiang, Hao Tan, Kai Zhang, Sai Bi, Tianyuan Zhang, Fujun Luan, Noah Snavely, and Zexiang Xu. Lvsm: A large view synthesis model with minimal 3d inductive bias. *arXiv preprint arXiv:2410.17242*, 2024. 2, 1, 3
- [21] HyunJun Jung, Nikolas Brasch, Jifei Song, Eduardo Perez-Pellitero, Yiren Zhou, Zhihao Li, Nassir Navab, and Benjamin Busam. Deformable 3d gaussian splatting for animatable human avatars. *arXiv preprint arXiv:2312.15059*, 2023. 2
- [22] Bernhard Kerbl, Georgios Kopanas, Thomas Leimkühler, and George Drettakis. 3d gaussian splatting for real-time radiance field rendering. *ACM Trans. Graph.*, 42(4):139–1, 2023. 1, 2, 3, 4, 6
- [23] Diederik P Kingma. Adam: A method for stochastic optimization. *arXiv preprint arXiv:1412.6980*, 2014. 1
- [24] Jiahui Lei, Yijia Weng, Adam Harley, Leonidas Guibas, and Kostas Daniilidis. Mosca: Dynamic gaussian fusion

- from casual videos via 4d motion scaffolds. *arXiv preprint arXiv:2405.17421*, 2024. 6
- [25] Lingzhi Li, Zhen Shen, Zhongshu Wang, Li Shen, and Ping Tan. Streaming radiance fields for 3d video synthesis. *Advances in Neural Information Processing Systems*, 35: 13485–13498, 2022. 2
- [26] Tianye Li, Mira Slavcheva, Michael Zollhoefer, Simon Green, Christoph Lassner, Changil Kim, Tanner Schmidt, Steven Lovegrove, Michael Goesele, Richard Newcombe, et al. Neural 3d video synthesis from multi-view video. In *Proceedings of the IEEE/CVF Conference on Computer Vision and Pattern Recognition*, pages 5521–5531, 2022. 6, 7, 3
- [27] Zhengqi Li, Wenqi Xian, Abe Davis, and Noah Snavely. Crowdsampling the plenoptic function. In *Computer Vision—ECCV 2020: 16th European Conference, Glasgow, UK, August 23–28, 2020, Proceedings, Part I 16*, pages 178–196. Springer, 2020. 2
- [28] Zhengqi Li, Simon Niklaus, Noah Snavely, and Oliver Wang. Neural scene flow fields for space-time view synthesis of dynamic scenes. In *Proceedings of the IEEE/CVF Conference on Computer Vision and Pattern Recognition*, pages 6498–6508, 2021. 2
- [29] Zhengqi Li, Qianqian Wang, Forrester Cole, Richard Tucker, and Noah Snavely. Dynibar: Neural dynamic image-based rendering. In *Proceedings of the IEEE/CVF Conference on Computer Vision and Pattern Recognition*, pages 4273–4284, 2023. 2
- [30] Zhan Li, Zhang Chen, Zhong Li, and Yi Xu. Spacetime gaussian feature splatting for real-time dynamic view synthesis. In *Proceedings of the IEEE/CVF Conference on Computer Vision and Pattern Recognition*, pages 8508–8520, 2024. 2
- [31] Hanxue Liang, Jiawei Ren, Ashkan Mirzaei, Antonio Torralba, Ziwei Liu, Igor Gilitschenski, Sanja Fidler, Cengiz Oztireli, Huan Ling, Zan Gojcic, et al. Feed-forward bullet-time reconstruction of dynamic scenes from monocular videos. *arXiv preprint arXiv:2412.03526*, 2024. 2
- [32] Yiqing Liang, Numair Khan, Zhengqin Li, Thu Nguyen-Phuoc, Douglas Lanman, James Tompkin, and Lei Xiao. Gaufré: Gaussian deformation fields for real-time dynamic novel view synthesis. *arXiv preprint arXiv:2312.11458*, 2023. 2
- [33] Yiqing Liang, Eliot Laidlaw, Alexander Meyerowitz, Srinath Sridhar, and James Tompkin. Semantic attention flow fields for monocular dynamic scene decomposition. In *Proceedings of the IEEE/CVF International Conference on Computer Vision*, pages 21797–21806, 2023. 2
- [34] Haotong Lin, Sida Peng, Zhen Xu, Yunzhi Yan, Qing Shuai, Hujun Bao, and Xiaowei Zhou. Efficient neural radiance fields for interactive free-viewpoint video. In *SIGGRAPH Asia 2022 Conference Papers*, pages 1–9, 2022. 2
- [35] Kai-En Lin, Lei Xiao, Feng Liu, Guowei Yang, and Ravi Ramamoorthi. Deep 3d mask volume for view synthesis of dynamic scenes. In *Proceedings of the IEEE/CVF International Conference on Computer Vision*, pages 1749–1758, 2021. 2
- [36] Wenbin Lin, Chengwei Zheng, Jun-Hai Yong, and Feng Xu. Occlusionfusion: Occlusion-aware motion estimation for real-time dynamic 3d reconstruction. In *Proceedings of the IEEE/CVF Conference on Computer Vision and Pattern Recognition*, pages 1736–1745, 2022. 2
- [37] Lu Ling, Yichen Sheng, Zhi Tu, Wentian Zhao, Cheng Xin, Kun Wan, Lantao Yu, Qianyu Guo, Zixun Yu, Yawen Lu, et al. DI3dv-10k: A large-scale scene dataset for deep learning-based 3d vision. In *Proceedings of the IEEE/CVF Conference on Computer Vision and Pattern Recognition*, pages 22160–22169, 2024. 5, 7, 1, 3
- [38] Stephen Lombardi, Tomas Simon, Jason Saragih, Gabriel Schwartz, Andreas Lehrmann, and Yaser Sheikh. Neural volumes: Learning dynamic renderable volumes from images. *arXiv preprint arXiv:1906.07751*, 2019. 2
- [39] Jonathon Luiten, Georgios Kopanas, Bastian Leibe, and Deva Ramanan. Dynamic 3d gaussians: Tracking by persistent dynamic view synthesis. In *2024 International Conference on 3D Vision (3DV)*, pages 800–809. IEEE, 2024. 2
- [40] Ben Mildenhall, Pratul P Srinivasan, Matthew Tancik, Jonathan T Barron, Ravi Ramamoorthi, and Ren Ng. Nerf: Representing scenes as neural radiance fields for view synthesis. *Communications of the ACM*, 65(1):99–106, 2021. 2, 3
- [41] Thomas Müller, Alex Evans, Christoph Schied, and Alexander Keller. Instant neural graphics primitives with a multiresolution hash encoding. *ACM transactions on graphics (TOG)*, 41(4):1–15, 2022. 2, 3
- [42] Richard A Newcombe, Dieter Fox, and Steven M Seitz. Dynamicfusion: Reconstruction and tracking of non-rigid scenes in real-time. In *Proceedings of the IEEE conference on computer vision and pattern recognition*, pages 343–352, 2015. 6
- [43] Keunhong Park, Utkarsh Sinha, Jonathan T Barron, Sofien Bouaziz, Dan B Goldman, Steven M Seitz, and Ricardo Martin-Brualla. Nerfies: Deformable neural radiance fields. In *Proceedings of the IEEE/CVF international conference on computer vision*, pages 5865–5874, 2021. 2, 3
- [44] Luigi Piccinelli, Yung-Hsu Yang, Christos Sakaridis, Mattia Segu, Siyuan Li, Luc Van Gool, and Fisher Yu. Unidepth: Universal monocular metric depth estimation. In *Proceedings of the IEEE/CVF Conference on Computer Vision and Pattern Recognition*, pages 10106–10116, 2024. 2
- [45] Julius Plucker. Xvii. on a new geometry of space. *Philosophical Transactions of the Royal Society of London*, pages 725–791, 1865. 4
- [46] Charles Ruizhongtai Qi, Li Yi, Hao Su, and Leonidas J Guibas. Pointnet++: Deep hierarchical feature learning on point sets in a metric space. *Advances in neural information processing systems*, 30, 2017. 6, 2
- [47] Zhiyin Qian, Shaofei Wang, Marko Mihajlovic, Andreas Geiger, and Siyu Tang. 3dgs-avatar: Animatable avatars via deformable 3d gaussian splatting. In *Proceedings of the IEEE/CVF conference on computer vision and pattern recognition*, pages 5020–5030, 2024. 2
- [48] René Ranftl, Katrin Lasinger, David Hafner, Konrad Schindler, and Vladlen Koltun. Towards robust monocular depth estimation: Mixing datasets for zero-shot cross-dataset transfer. *IEEE transactions on pattern analysis and machine intelligence*, 44(3):1623–1637, 2020. 2

- [49] René Ranftl, Alexey Bochkovskiy, and Vladlen Koltun. Vision transformers for dense prediction. In *Proceedings of the IEEE/CVF international conference on computer vision*, pages 12179–12188, 2021. 2
- [50] Christian Reiser, Stephan Garbin, Pratul Srinivasan, Dor Verbin, Richard Szeliski, Ben Mildenhall, Jonathan Barron, Peter Hedman, and Andreas Geiger. Binary opacity grids: Capturing fine geometric detail for mesh-based view synthesis. *ACM Transactions on Graphics (TOG)*, 43(4):1–14, 2024. 2
- [51] Jiawei Ren, Cheng Xie, Ashkan Mirzaei, Karsten Kreis, Zhiwei Liu, Antonio Torralba, Sanja Fidler, Seung Wook Kim, Huan Ling, et al. L4gm: Large 4d gaussian reconstruction model. *Advances in Neural Information Processing Systems*, 37:56828–56858, 2025. 2
- [52] Gernot Riegler and Vladlen Koltun. Free view synthesis. In *Computer Vision–ECCV 2020: 16th European Conference, Glasgow, UK, August 23–28, 2020, Proceedings, Part XIX 16*, pages 623–640. Springer, 2020. 2
- [53] Robin Rombach, Patrick Esser, and Björn Ommer. Geometry-free view synthesis: Transformers and no 3d priors. In *Proceedings of the IEEE/CVF International Conference on Computer Vision*, pages 14356–14366, 2021. 2
- [54] Mehdi SM Sajjadi, Henning Meyer, Etienne Pot, Urs Bergmann, Klaus Greff, Noha Radwan, Suhani Vora, Mario Lučić, Daniel Duckworth, Alexey Dosovitskiy, et al. Scene representation transformer: Geometry-free novel view synthesis through set-latent scene representations. In *Proceedings of the IEEE/CVF Conference on Computer Vision and Pattern Recognition*, pages 6229–6238, 2022. 2
- [55] Karen Simonyan and Andrew Zisserman. Very deep convolutional networks for large-scale image recognition. *arXiv preprint arXiv:1409.1556*, 2014. 8
- [56] Vincent Sitzmann, Michael Zollhöfer, and Gordon Wetzstein. Scene representation networks: Continuous 3d-structure-aware neural scene representations. *Advances in neural information processing systems*, 32, 2019. 2
- [57] Colton Stearns, Adam Harley, Mikaela Uy, Florian Dubost, Federico Tombari, Gordon Wetzstein, and Leonidas Guibas. Dynamic gaussian marbles for novel view synthesis of casual monocular videos. In *SIGGRAPH Asia 2024 Conference Papers*, pages 1–11, 2024. 2
- [58] Michael Steffen, Robert M Kirby, and Martin Berzins. Analysis and reduction of quadrature errors in the material point method (mpm). *International journal for numerical methods in engineering*, 76(6):922–948, 2008. 1
- [59] Mohammed Suhail, Carlos Esteves, Leonid Sigal, and Ameesh Makadia. Generalizable patch-based neural rendering. In *European Conference on Computer Vision*, pages 156–174. Springer, 2022. 2
- [60] Robert W Sumner, Johannes Schmid, and Mark Pauly. Embedded deformation for shape manipulation. In *ACM siggraph 2007 papers*, pages 80–es. 2007. 4, 6
- [61] Cheng Sun, Min Sun, and Hwann-Tzong Chen. Direct voxel grid optimization: Super-fast convergence for radiance fields reconstruction. In *Proceedings of the IEEE/CVF conference on computer vision and pattern recognition*, pages 5459–5469, 2022. 2
- [62] Jiakai Sun, Han Jiao, Guangyuan Li, Zhanjie Zhang, Lei Zhao, and Wei Xing. 3dstream: On-the-fly training of 3d gaussians for efficient streaming of photo-realistic free-viewpoint videos. In *Proceedings of the IEEE/CVF Conference on Computer Vision and Pattern Recognition*, pages 20675–20685, 2024. 2, 6, 3
- [63] Zhenggang Tang, Zhongzheng Ren, Xiaoming Zhao, Bowen Wen, Jonathan Tremblay, Stan Birchfield, and Alexander Schwing. Nerfdeformer: Nerf transformation from a single view via 3d scene flows. In *Proceedings of the IEEE/CVF Conference on Computer Vision and Pattern Recognition*, pages 10293–10303, 2024. 2
- [64] Zachary Teed and Jia Deng. Raft: Recurrent all-pairs field transforms for optical flow. In *Computer Vision–ECCV 2020: 16th European Conference, Glasgow, UK, August 23–28, 2020, Proceedings, Part II 16*, pages 402–419. Springer, 2020. 2
- [65] Richard Tucker and Noah Snavely. Single-view view synthesis with multipane images. In *Proceedings of the IEEE/CVF Conference on Computer Vision and Pattern Recognition*, pages 551–560, 2020. 2
- [66] Ashish Vaswani, Noam Shazeer, Niki Parmar, Jakob Uszkoreit, Llion Jones, Aidan N. Gomez, Lukasz Kaiser, and Illia Polosukhin. Attention is all you need, 2023. 4, 1
- [67] Qianqian Wang, Zhicheng Wang, Kyle Genova, Pratul P Srinivasan, Howard Zhou, Jonathan T Barron, Ricardo Martin-Brualla, Noah Snavely, and Thomas Funkhouser. Ibrnet: Learning multi-view image-based rendering. In *Proceedings of the IEEE/CVF conference on computer vision and pattern recognition*, pages 4690–4699, 2021. 2
- [68] Qianqian Wang, Vickie Ye, Hang Gao, Jake Austin, Zhengqi Li, and Angjoo Kanazawa. Shape of motion: 4d reconstruction from a single video. *arXiv preprint arXiv:2407.13764*, 2024. 2
- [69] Yiming Wang, Qin Han, Marc Habermann, Kostas Daniilidis, Christian Theobalt, and Lingjie Liu. Neus2: Fast learning of neural implicit surfaces for multi-view reconstruction. In *Proceedings of the IEEE/CVF International Conference on Computer Vision (ICCV)*, 2023. 2
- [70] Zhou Wang, Alan C Bovik, Hamid R Sheikh, and Eero P Simoncelli. Image quality assessment: from error visibility to structural similarity. *IEEE transactions on image processing*, 13(4):600–612, 2004. 7
- [71] Olivia Wiles, Georgia Gkioxari, Richard Szeliski, and Justin Johnson. Synsin: End-to-end view synthesis from a single image. In *Proceedings of the IEEE/CVF conference on computer vision and pattern recognition*, pages 7467–7477, 2020. 2
- [72] Suttisak Wizadwongsa, Pakkapon Phongthawee, Jiraphon Yenphraphai, and Supasorn Suwajanakorn. Nex: Real-time view synthesis with neural basis expansion. In *Proceedings of the IEEE/CVF Conference on Computer Vision and Pattern Recognition*, pages 8534–8543, 2021. 2
- [73] Guanjun Wu, Taoran Yi, Jiemin Fang, Lingxi Xie, Xiaopeng Zhang, Wei Wei, Wenyu Liu, Qi Tian, and Xinggang Wang. 4d gaussian splatting for real-time dynamic scene rendering. In *Proceedings of the IEEE/CVF conference on computer vi-*

- sion and pattern recognition*, pages 20310–20320, 2024. [2](#), [3](#), [6](#)
- [74] Wenqi Xian, Jia-Bin Huang, Johannes Kopf, and Changil Kim. Space-time neural irradiance fields for free-viewpoint video. In *Proceedings of the IEEE/CVF conference on computer vision and pattern recognition*, pages 9421–9431, 2021. [2](#)
- [75] Zhen Xu, Yinghao Xu, Zhiyuan Yu, Sida Peng, Jiaming Sun, Hujun Bao, and Xiaowei Zhou. Representing long volumetric video with temporal gaussian hierarchy. *ACM Transactions on Graphics*, 43(6), 2024. [2](#), [6](#), [7](#), [3](#)
- [76] Lihe Yang, Bingyi Kang, Zilong Huang, Xiaogang Xu, Jiashi Feng, and Hengshuang Zhao. Depth anything: Unleashing the power of large-scale unlabeled data. In *Proceedings of the IEEE/CVF Conference on Computer Vision and Pattern Recognition*, pages 10371–10381, 2024. [2](#)
- [77] Ziyi Yang, Xinyu Gao, Wen Zhou, Shaohui Jiao, Yuqing Zhang, and Xiaogang Jin. Deformable 3d gaussians for high-fidelity monocular dynamic scene reconstruction. In *Proceedings of the IEEE/CVF conference on computer vision and pattern recognition*, pages 20331–20341, 2024. [3](#)
- [78] Alex Yu, Vickie Ye, Matthew Tancik, and Angjoo Kanazawa. pixelnerf: Neural radiance fields from one or few images, 2021. [2](#)
- [79] Kai Zhang, Sai Bi, Hao Tan, Yuanbo Xiangli, Nanxuan Zhao, Kalyan Sunkavalli, and Zexiang Xu. Gs-lrm: Large reconstruction model for 3d gaussian splatting. In *European Conference on Computer Vision*, pages 1–19. Springer, 2025. [1](#), [2](#), [3](#), [4](#), [5](#), [6](#), [7](#)
- [80] Richard Zhang, Phillip Isola, Alexei A Efros, Eli Shechtman, and Oliver Wang. The unreasonable effectiveness of deep features as a perceptual metric. In *Proceedings of the IEEE conference on computer vision and pattern recognition*, pages 586–595, 2018. [7](#)
- [81] Richard Zhang, Phillip Isola, Alexei A Efros, Eli Shechtman, and Oliver Wang. The unreasonable effectiveness of deep features as a perceptual metric. In *CVPR*, 2018. [5](#)
- [82] Tinghui Zhou, Richard Tucker, John Flynn, Graham Fyffe, and Noah Snavely. Stereo magnification: Learning view synthesis using multiplane images. In *SIGGRAPH*, 2018. [2](#), [5](#), [7](#), [1](#), [6](#)

SplatVoxel: History-Aware Novel View Streaming without Temporal Training

Supplementary Material

A. Implementation Details

Our framework is implemented in JAX [3] and trained on NVIDIA A100 GPUs. We evaluate the speed of both GS-LRM and our method on a single NVIDIA H100 GPU. We evaluate the speed of other optimization-based baselines, including 3DGS, 3DGStream, and 4DGS, on a single NVIDIA A100 GPU due to limitations with the H100 card. While running on an H100 can offer speed improvements, these baselines remain constrained by their inherent computational complexity and fail to achieve 1FPS.

We use the Adam optimizer [23] with an initial learning rate of $4e-4$, applying cosine learning rate decay with linear warmup. The warmup period is set to 5000 training steps.

A.1. Network Structure

Our network consists of a *Multi-view Transformer* backbone and a *Sparse Voxel Transformer*. The multi-view transformer has 24 transformer layers with 1024 hidden dimensions and 16 attention heads. The sparse voxel transformer uses 6 layers with 128 hidden dimensions and 8 attention heads. To demonstrate the effectiveness of our representation, we use a 12-layer multi-view transformer in Table 4, showing that it can outperform GS-LRM by 2dB in PSNR while maintaining a comparable network capacity and similar inference time.

Each transformer layer [66] consists of a self-attention mechanism and feed-forward networks, with all bias terms removed following GS-LRM [79]. Additionally, following LVSM [20], we incorporate QK-Norm [16] to stabilize training. For efficiency, we utilize the CUDNN-FlashAttention [9] implementation available in Jax.

The shallow multi-layer perceptrons MLP_{coarse} and MLP_{fine} share similar structures with the feed-forward network in a transformer layer. It includes two linear layers with a LayerNorm [1] and GeLU [15] activation function, and an additional residual connection.

A.2. Hybrid Splat-Voxel Representation

Our SplatVoxel model is inspired by Lagrangian-Eulerian representations in physical simulation where we combine the gaussian splats (Lagrangian representation) and voxels (Eularian representation) to assist warping and fusion of history information.

We use the official splatting-based rasterizer from 3D Gaussian Splatting [22] to render images from predicted Gaussian primitives. To ensure a fair comparison with GS-LRM on RealEstate10K[82], we set the spherical harmonics degree to 0 for Table 6. For models trained on the

DL3DV dataset [37], the degree is set to 1 to enhance view-dependent effects.

Our voxel grid is aligned with the target camera, and is in the normalized device space (NDC), where the z-axis is linear in disparity. This space is helpful in presenting unbounded, in-the-wild scenes. The full fine volume size is set to $[64, H, W]$, where the H, W corresponds to the rendered image height and width. The coarse volume size is set to $[32, H//8, W//8]$, meaning each coarse-level volume is subdivided into $[2, 8, 8]$ fine-level volumes.

We initialize the voxels by depositing the Gaussian primitives to the volume with a 3D distance-based kernels used in Material Point Method [58]:

$$\mathcal{K}(\mathbf{x}) = K\left(\frac{x}{h}\right) K\left(\frac{y}{h}\right) K\left(\frac{z}{h}\right), \quad (12)$$

where $\mathbf{x} = (x, y, z)$ is the offset from the voxel center to the Gaussian primitive center, and h is the grid size used to normalize the offset vector to the range $[-1, 1]$. The function $K(x)$ is a one-dimensional cubic kernel function given by:

$$K(x) = \frac{1}{6}(3|x|^3 - 6x^2 + 4) \quad (13)$$

Rather than directly generating new attributes, we design the voxel transformer to predict residuals that are added to the initial Gaussian rendering attributes on voxels. Specifically, given the input fine-level voxel attributes obtained through the Splat Fusion procedure \mathbf{E}_j which comprise the fused splat feature \mathbf{F}_j and rendering parameters \mathbf{G}_j through the Splat Fusion procedure, the transformer obtain the final splat rendering parameters \mathbf{G}'_j in Eqn. 7 as:

$$\begin{aligned} \Delta \mathbf{G}_j &= \text{MLP}_{fine}([\mathbf{O}_j, \mathbf{E}_j]) \\ \mathbf{G}'_j &= \mathbf{G}_j + \Delta \mathbf{G}_j. \end{aligned} \quad (14)$$

A.3. 3D Warping

Triangulation We use TAPIR [10] as our 2D tracking backbone, which takes query points and video frames as input and produces 2D tracking positions throughout the video with the corresponding occlusion mask, indicating whether a tracked point is visible in a given frame. In addition to the occlusion mask obtained from 2D tracking, the visibility mask γ_i used in Eqn. 10 for triangulation also depends on depth-based visibility. Depth-based visibility is determined by comparing the projected depth of a given splat with the depth map obtained by rendering all splats to a given view. If the projected depth is smaller, the splat is considered unoccluded. This process utilizes alpha blending of

splat depths to derive rendered depths from 3D Gaussian Splatting, a widely adopted technique that has been demonstrated to be effective [7].

Embedded Deformation Graph Assuming motion continuity between neighboring frames, we first estimate optical flow between each keyframe and its subsequent frame using RAFT [64] to identify regions of significant movement. We select regions within the input views where the optical flow norm exceeds a threshold of 0.2 pixels as areas of significant motion. Each splat is then projected onto the input views to determine whether its projected position falls within these significant motion regions and remains unoccluded based on the depth-based visibility verification aforementioned. If a splat exhibits significant motion in more than half of the views, it is prioritized for sampling as an anchor splat. During experiments, we found that uniformly sampling 512 points from the prioritized splats using the Farthest Point Sampling method [46] is sufficient for effectively handling moving Gaussians in the keyframes.

The deformation of each splat is computed using Linear Blend Skinning (LBS) based on the deformation of its associated anchor splats. For each Gaussian, we employ a K-nearest neighbors approach with $k = 4$ to identify the closest anchor splats. The position displacement $\delta\mathbf{p} \in \mathbb{R}^3$ is then determined by blending the deformations of the selected anchor points, denoted as $\mathbf{t}_i \in \mathbb{R}^3$.

$$\delta\mathbf{p} = \sum_{i=1}^k w_i \mathbf{t}_i \quad (15)$$

$$w_i = \frac{\exp(-\|d_i\|^2/\sigma^2)}{\sum_{j=1}^k \exp(-\|d_j\|^2/\sigma^2)},$$

where d_i represents the Euclidean distance between the Gaussian primitive and the i -th anchor point, while σ controls the smoothness of the weighting function, set to the mean distance between anchor points and the querying splats. To ensure that static splats remain unaffected, we set displacement $\delta\mathbf{p}$ to be zero if the distance to the anchors is greater than $\lambda\bar{d}$, where \bar{d} is the mean distance between anchor points and λ is a hyperparameter controlling the motion graph’s extent. In practice we set λ between 0.2 to 0.5 depending on the scene.

Error-aware Temporal Fusion Static areas are identified during the Splat-to-voxel transfer process, where historical splats undergoing deformation mark their neighboring voxels as regions of motion.

B. Two-stage training

Our training procedure first trains the multi-view transformer portion, and then jointly trains the multi-view trans-

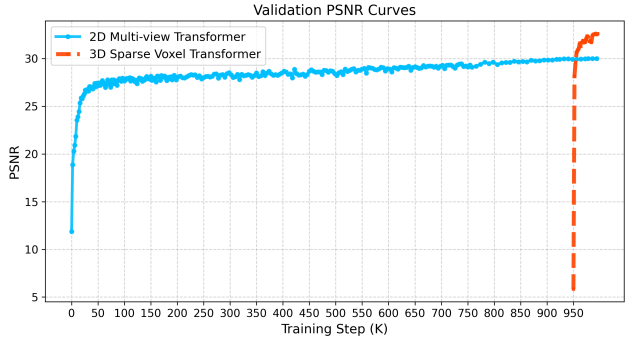


Figure 7. **Comparison of Multi-View and Voxel Transformers.** Validation curves of our transformer variations on the DL3DV dataset. Compared to the Multi-view transformer which produces gaussian primitives aligned with the 2D input images, our Sparse Voxel Transformer is able to converge at a better result within very few training steps.

Table 6. **Reproduced GS-LRM Performance.** Our reproduced GS-LRM achieves improved LPIPS and SSIM scores with a slight decrease in PSNR on the RealEstate10K dataset compared to the officially reported numbers.

| Method | PSNR \uparrow | SSIM \uparrow | LPIPS \downarrow |
|------------------------|-----------------|-----------------|--------------------|
| pixelNeRF [78] | 20.43 | 0.589 | 0.550 |
| GPNR [59] | 24.11 | 0.793 | 0.255 |
| Du et al. [12] | 24.78 | 0.820 | 0.213 |
| pixelSplat [5] | 26.09 | 0.863 | 0.136 |
| MVSplat [6] | 26.39 | 0.869 | 0.128 |
| GS-LRM (Official) [79] | 28.10 | 0.892 | 0.114 |
| GS-LRM (Reproduced) | 27.78 | 0.902 | 0.082 |
| Ours | 28.47 | 0.907 | 0.078 |

former with the voxel transformer. As shown in the training curves 7, our proposed voxel transformer efficiently reasons about 3D information, surpassing the performance of only using the multi-view transformer with the same number of steps.

C. Dataset

C.1. Static Scene Datasets

RealEstate10K [82] For the RealEstate10K dataset, we set the training and testing resolution to 256×256 . Both GS-LRM and our model are trained for 100K iterations. Specifically, we first train our multi-view transformer backbone for 80K iterations, followed by 20K iterations of joint training with the voxel decoder. Each training batch consists of two input views and six target views with a baseline of one unit length between the input views, following the training setup of GS-LRM. For evaluation, we use the same input and target indices as PixelSplat and GS-LRM.

Table 7. Quantitative evaluation comparing our method with the best-performing baselines, 4DGS [73] and GS-LRM [79], across all sequences in LongVolumetricVideo [75] and Neural3DVideo [26]. The **best** and **second-best** results are highlighted for clarity.

| Dataset | Sequence | 4DGS | | | | GS-LRM | | | | Ours | | | |
|------------|-------------------------|-----------------|-----------------|--------------------|----------------------|-----------------|-----------------|--------------------|----------------------|-----------------|-----------------|--------------------|----------------------|
| | | PSNR \uparrow | SSIM \uparrow | LPIPS \downarrow | Flicker \downarrow | PSNR \uparrow | SSIM \uparrow | LPIPS \downarrow | Flicker \downarrow | PSNR \uparrow | SSIM \uparrow | LPIPS \downarrow | Flicker \downarrow |
| LongVolCap | <i>Corgi</i> | 17.25 | 0.530 | 0.423 | 8.17 | 26.24 | 0.882 | 0.118 | 9.95 | 26.48 | 0.885 | 0.109 | 8.76 |
| | <i>Bike</i> | 20.26 | 0.742 | 0.288 | 4.89 | 24.74 | 0.830 | 0.158 | 6.97 | 24.64 | 0.844 | 0.140 | 6.80 |
| Neural3DV | <i>coffee_martini</i> | 19.29 | 0.676 | 0.268 | 1.83 | 20.86 | 0.801 | 0.149 | 7.21 | 23.10 | 0.832 | 0.126 | 2.33 |
| | <i>cut_roasted_beef</i> | 25.41 | 0.851 | 0.167 | 3.17 | 21.95 | 0.855 | 0.134 | 5.51 | 29.15 | 0.909 | 0.096 | 3.26 |
| | <i>flame_steak</i> | 26.54 | 0.854 | 0.159 | 3.24 | 22.04 | 0.866 | 0.121 | 5.56 | 29.10 | 0.903 | 0.100 | 3.31 |
| | <i>cook_spinach</i> | 24.41 | 0.794 | 0.198 | 3.49 | 21.93 | 0.872 | 0.119 | 5.78 | 29.26 | 0.906 | 0.103 | 3.42 |
| | <i>flame_salmon_1</i> | 19.92 | 0.709 | 0.250 | 2.18 | 21.70 | 0.827 | 0.126 | 5.65 | 24.70 | 0.860 | 0.102 | 2.52 |
| | <i>sear_steak</i> | 23.42 | 0.804 | 0.206 | 2.52 | 22.23 | 0.869 | 0.122 | 4.92 | 29.14 | 0.907 | 0.098 | 2.64 |

DL3DV [37] For the DL3DV dataset, we set the training and testing resolution to 384×216 . For training, we randomly select one image in the scene as the target, and randomly select four of the nearest eight cameras to the target as inputs. We scale the scene such that the cameras fit within a unit cube. For evaluation, we use every eighth image as the target set, and for each target we use the nearest four cameras not in the target set as inputs. We average metrics per scene, and then average over all scenes. In our experiments on the DL3DV test set (Table 4), both our model and GS-LRM are trained using 8 GPUs, with a batch size of 2 per GPU, for a total of 200K iterations. We first train the multi-view transformer backbone for 100K iterations, followed by 100K iterations of joint training with the voxel decoder.

For cross-dataset evaluation on dynamic scene datasets, we train both GS-LRM and our model on DL3DV using a batch size of 128, for a total of 300K iterations. The training follows a two-stage process: we first train the multi-view transformer backbone for 200K iterations, then jointly train the voxel decoder for 100K iterations.

C.2. Dynamic Scene Datasets

Neural3DVideo [26] We use six sequences from the dataset for evaluation. The center target camera is selected as the evaluation view, while the two second-closest cameras on either side are used as input cameras. We use resolution 320×240 downsampling from their original resolution.

LongVolumetricVideo [75] For evaluation, we use the Corgi and Bike sequences and select a 4-input-camera setup that covers one target view. We failed to find enough baseline coverage for other sequences in LongVolCap using only 4 input cameras. For both the Corgi and Bike sequences, we use 1500 frames for evaluation.

We use resolution 384×216 for Corgi and 256×256

for the Bike sequences, downsampling from their original resolution.

D. Baselines

3DGS We use the original 3D Gaussian Splatting implementation [22], and reduce the number of training iterations from original 30,000 to 1,000 for *Neural3DVideo* and 1,500 for *LongVolumetricVideo*. This modification not only accelerates training but also significantly enhances novel view synthesis results (e.g. around 4 PSNR improvement). Given the sparsity of the input data, this adjustment is crucial for preventing overfitting. All other parameters are kept consistent with the original implementation.

3DGStream We use the open-source 3DGStream [62] implementation to process the multi-view videos. We first use the original 3DGS to optimize on the first frame for 1,500 iterations, warmup the NTC cache, and then optimize on the next frame using the previous 3DGS for 150 iterations, following the original implementation.

4DGS We use the open-source 4DGS [73] implementation to process the multi-view videos. Following their implementation, we first optimized the first frame for 3,000 iterations, and then optimize on the full multi-view video sequence for 14,000 iterations.

GS-LRM We enhance GS-LRM’s speed by replacing the CNN deconvolution with an MLP unpatchify layer as proposed in [20], and implementing it in JAX. We maintain the same network parameters and training loss weights as in the original paper. Additionally, we use the LPIPS loss employed in our model, achieving improved LPIPS and SSIM scores, with a slight decrease in PSNR, as detailed in Table 2. We adopt the same color modeling approach as the official paper for RealEstate10K, setting the spherical harmonics degree to 0. For the GS-LRM baseline trained on

DL3DV, we set the degree to 1 to ensure a fair comparison with our method. Additionally, we found that this modification enhances GS-LRM’s performance on DL3DV.

E. Additional Results

Novel View Streaming Table 7 presents detailed metrics for our results alongside the two best-performing baselines, 4DGS and GS-LRM, evaluated across all eight sequences.

Feed-forward Novel View Synthesis We also provide additional examples comparing GS-LRM with our method on both DL3DV and RealEstate10K, as shown in Fig. 8 and Fig. 9.

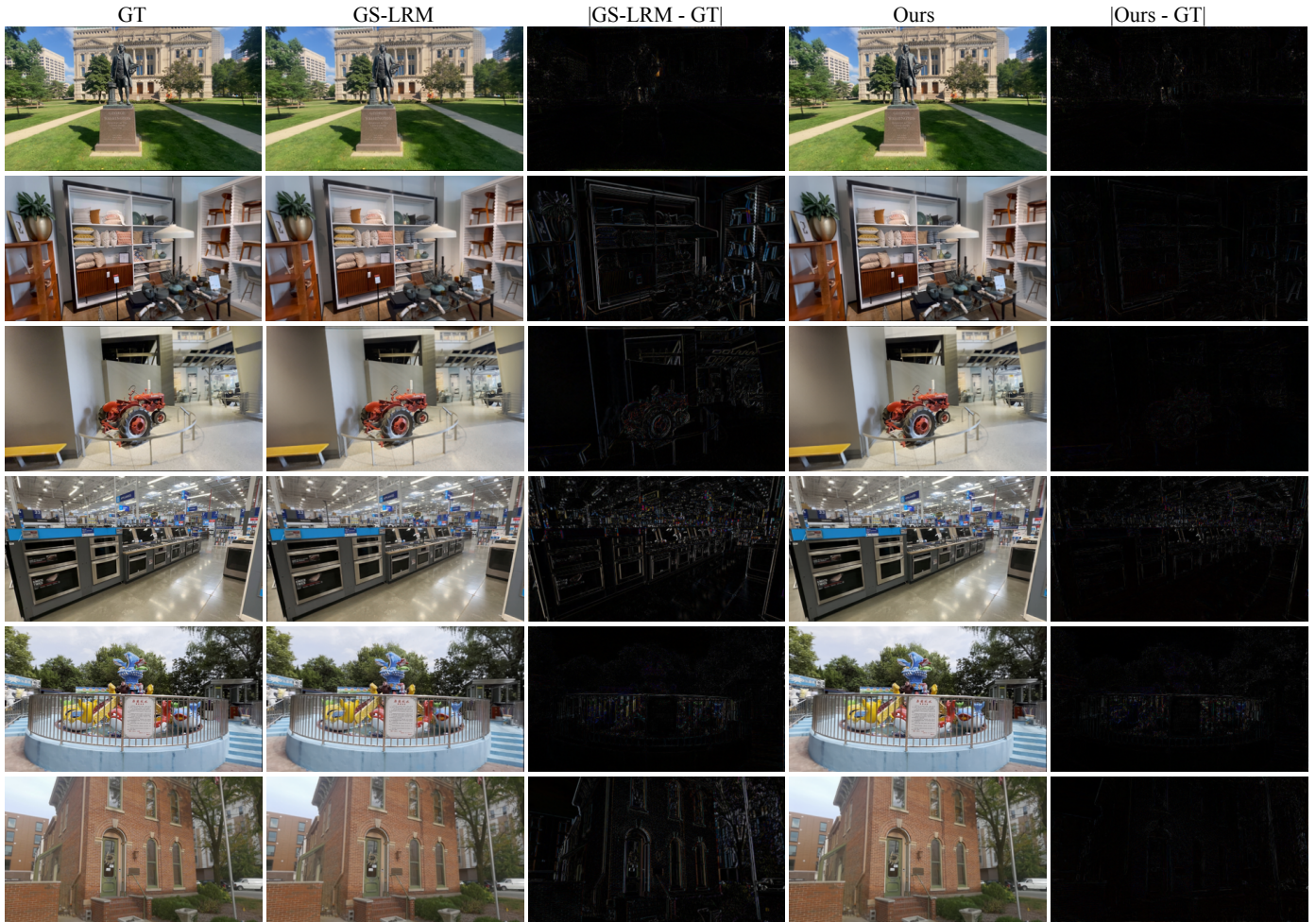


Figure 8. **DL3DV Static Scene Reconstruction.** Additional qualitative examples of GS-LRM and our method trained on DL3DV.



Figure 9. **Re10K Static scene reconstruction.** Additional qualitative examples of GS-LRM trained on RealEstate10k [82].